JACS
JOURNAL OF THE AMERICAN CHEMICAL SOCIETY
pubs.acs.org/JACS
Article

Pinpointing Chemomechanical Origins of Na Cathode Degradation

Tianxiao Sun,[○] Bin Wu,[*,○] Shimao Deng,[○] Yu-Jie Guo, Ji-Lei Shi, Xing Zhang, Xiaofeng Shi, Guannan Qian, Jian Wang, Piero Pianetta, Jigang Zhou,[*] Yu-Guo Guo,[*] and Yijin Liu[*]

Cite This: *J. Am. Chem. Soc.* 2025, 147, 21375−21384

Read Online

ACCESS | Metrics & More | Article Recommendations | Supporting Information

ABSTRACT: The performance and longevity of sodium-ion batteries are heavily influenced by cathode degradation, particularly under high-voltage cycling. Despite ongoing research, the interplay between chemical and mechanical processes remains unclear. Here, we investigated the degradation mechanisms of an O3-$NaLi_{1/9}Ni_{2/9}Fe_{2/9}Mn_{4/9}O_2$ (NLNFM) cathode material using synchrotron-based nanoresolution chemical imaging. Oxygen loss at high voltages was identified as the primary trigger, causing unwanted phase transformations, disrupting sodium intercalation, and leading to capacity fade. Fluorine incorporation during cycling also induced stress and particle cracking, accelerating degradation. By analyzing particles of different sizes, we revealed distinct degradation pathways: small particles experience severe side reactions during early cycling due to their high specific surface area, while large particles develop progressive structural damage during extended cycling from intraparticle heterogeneity and stress. These findings highlight the particle-size-dependent nature of cathode degradation and inform strategies such as particle size optimization, doping, micromorphology design, and stress-tolerant structures to mitigate capacity fade in sodium-ion batteries.

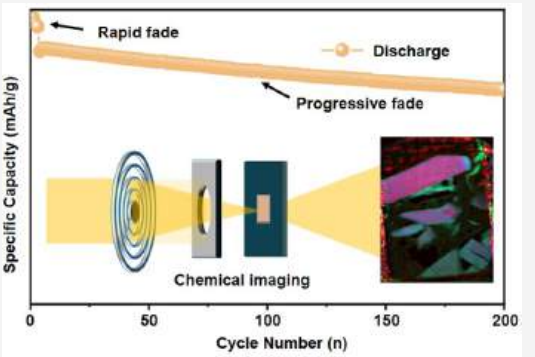

Downloaded via UNIV OF TEXAS AT AUSTIN on July 2, 2025 at 16:16:03 (UTC).
See https://pubs.acs.org/sharingguidelines for options on how to legitimately share published articles.

INTRODUCTION

Lithium-ion batteries, through extensive research and development over the past few decades, have greatly enhanced everyday life.[1−4] However, factors such as geographical distribution, abundance, and cost have raised concerns about sustainability and, thus, led to increasing interest in sodium-ion batteries (SIBs).[5−7] Among the various candidates reported, O3-type layered transition metal oxides (Na_xTMO_2, where $0.67 < x \leq 1$; TM = transition metals) have garnered significant attention from both academia and industry due to their outstanding theoretical capacity, tunable operating voltage, straightforward synthesis, and low cost.[8,9] In practical applications, the high energy density resulting from dual redox reactions (involving TM cations and O anions) is accompanied by detrimental phenomena, including capacity fade and voltage hysteresis, as well as safety issues such as cell deformation, swelling, and excessive heat generation.[10] During the operation of O3-Na_xTMO_2 cathodes, typically at voltages >4.0 V (vs Na^+/Na), unwanted processes such as irreversible phase transitions, lattice distortion, volume expansion, gas evolution, and crack formation have been experimentally observed and associated with cathode degradation.[11−16]

Although the detailed mechanisms are still debated, substantial evidence has been presented linking the degradation to the irreversible continuous O′3-P′3-P″3-O″3-O‴3 phase transitions in O3-Na_xTMO_2.[11,17] By incorporating Li ions into the TM layers of a Na_xTMO_2 material ($Na_{0.85}Li_{0.1}Ni_{0.175}Mn_{0.525}Fe_{0.2}O_2$), our earlier research successfully improved the reversibility of the O3-P3 phase transition by mitigating the Jahn−Teller (J-T) distortion of Ni^{3+} and thus suppressing the undesirable loss of active mass during high-voltage charge compensation that involves anion redox.[18] However, structural degradation and poor electrochemical performance are still reported in these Li-doped Na_xTMO_2 materials upon charging to high voltages (>4.0 V). Evidence suggests that irreversible oxygen redox at high voltages is often accompanied by the formation of oxygen gas and the progressive reduction and dissolution of TM ions from the layered sodium oxide cathodes.[19−21] This process leads to the reconstruction of the electronic and crystallographic structures in a highly heterogeneous fashion, affecting Na intercalation and causing capacity fade.

Additionally, cathode degradation in SIB has been linked to the corrosive effects of hydrofluoric acid (HF) in the electrolyte.[22,23] Trace water in carbonate solvents could react with $NaPF_6$, forming HF. Moreover, electrochemical reactions at high voltages can also produce HF. Anionic redox reactions generate various intermediate states of oxygen ions, which could cause the decomposition of solvents in the electrolyte.

Received: October 17, 2024
Revised: June 3, 2025
Accepted: June 4, 2025
Published: June 10, 2025

ACS Publications
© 2025 American Chemical Society

https://doi.org/10.1021/jacs.4c14571
J. Am. Chem. Soc. 2025, 147, 21375−21384

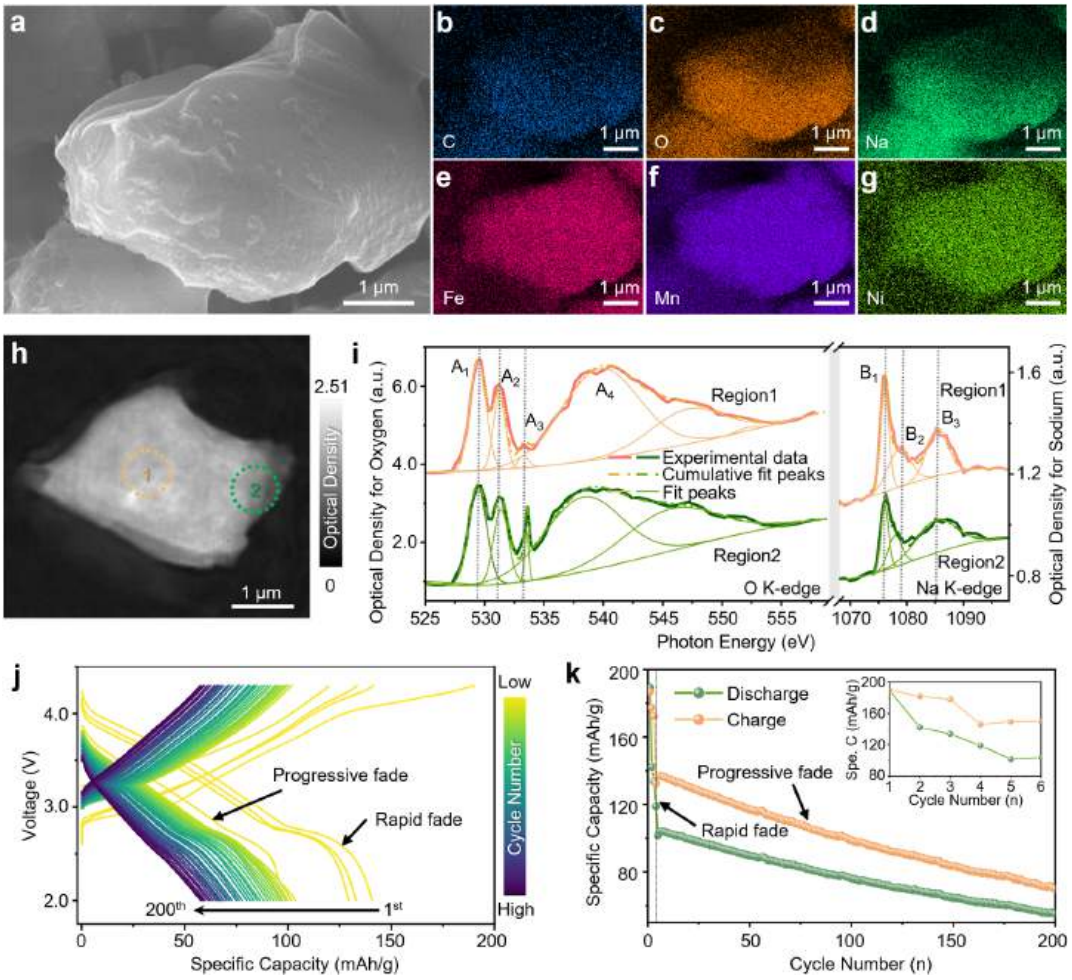

Figure 1. (a) The SEM image of O3-type $NaLi_{1/9}Ni_{2/9}Fe_{2/9}Mn_{4/9}O_2$ cathode pristine particles. (b–g) EDS elemental maps of the same region as (a), showing the distribution of C, O, Na, Fe, Mn, and Ni, respectively. (h) Averaged ptychography amplitude image of an O3-type $NaLi_{1/9}Ni_{2/9}Fe_{2/9}Mn_{4/9}O_2$ cathode pristine particle from the O K-edge, Mn $L_{2,3}$-edge, Fe $L_{2,3}$-edge, Ni $L_{2,3}$-edge, and Na K-edge. (i) The absorption spectra of the O K-edge and Na K-edge in region 1 (yellow) and region 2 (green) of (h). (j) The galvanostatic charge/discharge voltage profiles at 1 C. (k) The cycling performance at 1 C.

The decomposition products (such as ClO_4^- and PF_6^- in ethylene carbonate, EC) further catalyze the breakdown of the electrolyte solvent EC into CO_2 and acetaldehyde radicals ($O_2^{\bullet-}$), ultimately promoting HF formation through $LiPF_6$ hydrolysis. Consequently, HF leaches TM ions from the cathode surface, forming a high-impedance TMF_2 interphase, contributing to metal cation loss and capacity fade. The specific role of F in this process remains unclear and requires further investigation.

Another contributing factor to the degradation of SIB cathodes is the accumulation of mechanical stress, often manifested through the formation of microcracks.[24] Even in a well-formed electrode, cathode particles can exhibit considerable variations in their chemical onset, reaction rates, and states of charge (SoC). These discrepancies result in the formation of microreaction regions that are not uniform or coherent with one another. The mechanical stress arising from these heterogeneous microregions accumulates over time, leading to the development of cracks across different length scales. These cracks form new interfaces between the electrode and electrolyte, further exacerbating cathode degradation. Our previous work elucidated the structural and chemical complexity of lithium-based layered oxide cathodes following a designed electrochemical cycling procedure.[25] However, the intrinsic mechanisms of performance degradation in sodium-ion batteries, especially those coupling chemical and mechanical dynamics, have not been well studied. It is scientifically interesting and practically important to establish an understanding of the link between the molecular-scale chemical and physical behaviors of SIB materials and key macroscopic performance metrics, such as capacity fade and lifespan.

Spatially resolved X-ray absorption spectroscopy (XAS) techniques, such as STXM, photoemission electron microscopy (PEEM), and transmission X-ray microscopy (TXM), have been extensively utilized to investigate battery materials.[26−28] These methods enable the determination of material structures, chemical or charge distributions, and chemo-mechanical degradation processes. Among these, STXM-based ptychography, which combines X-ray diffraction microscopy (XDM) with STXM, offers high spatial resolution, high chemical sensitivity, and low radiation dose using a defocused beam spot for chemical mapping of different chemical species.

In this work, we carried out a systematic investigation of a Li-doped Na layered oxide cathode (O3-Na-

https://doi.org/10.1021/jacs.4c14571
J. Am. Chem. Soc. 2025, 147, 21375−21384

$Li_{1/9}Ni_{2/9}Fe_{2/9}Mn_{4/9}O_2$) as a model system. Both conventional spectro-STXM and high-spatial-resolution ptychography were conducted for functionally important elements, including O, Mn, Ni, Fe, F, and Na, to quantitatively analyze the electrochemical heterogeneity and asynchronicity in the cathode material during cycling. We delved into the chemo-mechanical origins of cathode degradation in sodium-ion batteries. Our findings reveal that the degradation of NLNFM cathode materials is driven by the interplay between chemical and mechanical factors, with a notable particle size dependence. Larger particles initially degrade more slowly due to their relatively low surface area, while smaller particles experience severe side reactions during the formation process. Upon long-term cycling, significant intraparticle heterogeneity and mechanical strain develop in larger particles. The primary cause of degradation is the loss of oxygen at high voltages, which leads to the migration of Mn^{4+} and disrupts the Na^+ intercalation process. Additionally, fluorine becomes incorporated into the lattice upon long-term cycling, forming NaF nanoparticles, which induce local stress and cause structural disintegration. These findings emphasize the need to enhance the stability and robustness of sodium-ion batteries through a multiscale codesign strategy, involving processes such as particle size control, doping, morphology optimization, and surface coating.

RESULTS AND DISCUSSION

The Li-doped Na-ion battery cathode material, O3-Na$Li_{1/9}Ni_{2/9}Fe_{2/9}Mn_{4/9}O_2$ (NLNFM), was prepared via solid-state reactions (Figure S1). The details of the synthesis protocol are provided in the Methods section. Scanning electron microscopy (SEM) and energy-dispersive spectroscopy (EDS) images of the pristine cathode particles (Figures 1a–g andS2) show a relatively uniform morphology and elemental distribution. The unexpected presence of carbon in the pristine material may be due to air exposure during sample handling and necessitates further investigation. To supplement the SEM-EDS technique, which is known for its limited sensitivity and penetration depth, we conducted STXM-based spectro-ptychography on a randomly selected pristine NLNFM particle. Figure 1h illustrates the averaged amplitude image obtained through spectro-ptychography at various X-ray absorption edges, namely the O K-edge, Mn $L_{2,3}$-edge, Fe $L_{2,3}$-edge, Ni $L_{2,3}$-edge, and Na K-edge. The pixel values were converted to optical density (OD), which is proportional to the sample thickness along the beam direction. To evaluate the chemical heterogeneity, two regions of interest were selected in the core (region 1) and near the surface (region 2) of this particle, respectively. The corresponding O K-edge and Na K-edge spectra obtained from spectro-ptychography demonstrate significant discrepancies. The O K-edge absorption spectra (left of Figure 1i) exhibit four prominent oscillation features. Peaks A_1 and A_2 are attributed to the electronic transition from O 1s to 2p orbitals, which covalently hybridize with the t_{2g} and e_g states of the transition metal (TM) 3d orbitals.[29,30] The distinctive oscillating structure of A_3 arises from the contribution of CO_3^{2-} species.[31] The higher A_3 peak intensity in region 2 indicates that the particle edge demonstrates a higher concentration of CO_3^{2-} salts compared with core region 1. The detection of CO_3^{2-} species is consistent with the presence of C detected by SEM-EDS. Peak A_4 at above 535 eV primarily corresponds to the electronic transition from the O 1s core state to the hybrid state of O 2p-TM 4s and 4p orbitals.[29]

A closer observation shows that the edge jumps of the O spectrum are 2.86 for region 2 and 2.59 for region 1. Meanwhile, the A_1 peak intensity for region 1 (2.73) is higher than that for region 2 (2.51). Furthermore, the full width at half maximum (fwhm) of peaks A_2 and A_4 increases from 1.2 and 10.2 eV in region 1 to 1.8 and 11.1 eV in region 2, respectively. The A_2 and A_3 peak positions also shift from 531.2 and 533.2 eV in region 1 to 531.5 and 533.7 eV in region 2, respectively. These observations suggest that the carbonate species in the reconstructed surface not only enhance the complexity of the oxygen chemical environment, such as variations in TM species and quantity, but also reduce the covalent strength of the O-TM bonds in that region.

On the other hand, the Na K-edge spectra exhibit three main oscillation characteristics. The prominent peaks B_1 and B_3 correspond to the electronic transition from the Na 1s core state to the two Na 3p states, which experience splitting within the crystal field.[31] Peak B_2 primarily involves the electronic transition from Na 1s to the Laporte-forbidden t_{2g}-like state, split by the Na 3d energy level.[32] This may be linked to the formation of sodium carbonate.[33,34] Similar to the oxygen spectrum, the edge jump in region 2 is 0.17 compared to 0.14 in region 1, indicating a higher Na concentration in region 2. However, the peak intensities of B_1, B_2, and B_3 in region 2 (0.27, 0.14, and 0.21, respectively) are lower than those in region 1 (0.41, 0.19, and 0.22, respectively). Moreover, the peak positions of B_1 and B_2 shift from 1076.0 and 1085.2 eV in region 1 to 1076.4 and 1086.1 eV in region 2, respectively. The fwhm of B_1 and B_2 broadens from 1.9 and 5.5 eV in region 1 to 2.1 and 9.8 eV in region 2, respectively. Notably, the peak position of B_2 decreases from 1079.1 eV in region 1 to 1077.9 eV in region 2. These observations suggest a distinct trade-off between the Na K-edge and the O K-edge features, which may reflect differing sodium environments in the two regions. In region 1, the spectra are dominated by intercalated Na, as evidenced by the strong and sharp B_1 peak, indicating a more crystalline and well-ordered sodium phase. In contrast, region 2 is dominated by sodium carbonate, which is characterized by a strong and sharp A_3 feature in the O K-edge spectra. The diminished B_1 feature in this region implies that the Na ions are associated with the carbonate in a less crystalline or more disordered structure. Therefore, the presence of Na_2CO_3 may suggest sodium loss due to exposure to air (likely initiated in ethanol dispersions). This process does not involve the oxidation of the transition metals (as demonstrated in Figure S3). Nonetheless, it can alter the covalent strength of TM-O bonds, resulting in correlated variations between the Na and O spectra, demonstrating that the highly sensitive O and Na spectra serve as useful fingerprints for the chemical behavior in the cathode.

To investigate the cycling performance of this material, we fabricated coin cells and conducted 200 cycles of cyclic voltammetry charge–discharge testing. Figure 1j,k shows the galvanostatic charge/discharge voltage profiles and the cycling performance at 1 C, respectively. The initial formation cycles involve a complex activation process of the cathode, exhibiting a significant decrease in specific capacity. Afterward, the decline becomes more gradual, which clearly suggests that different degradation processes are at play during the initial formation cycles compared with the subsequent ones.

https://doi.org/10.1021/jacs.4c14571
J. Am. Chem. Soc. 2025, 147, 21375–21384

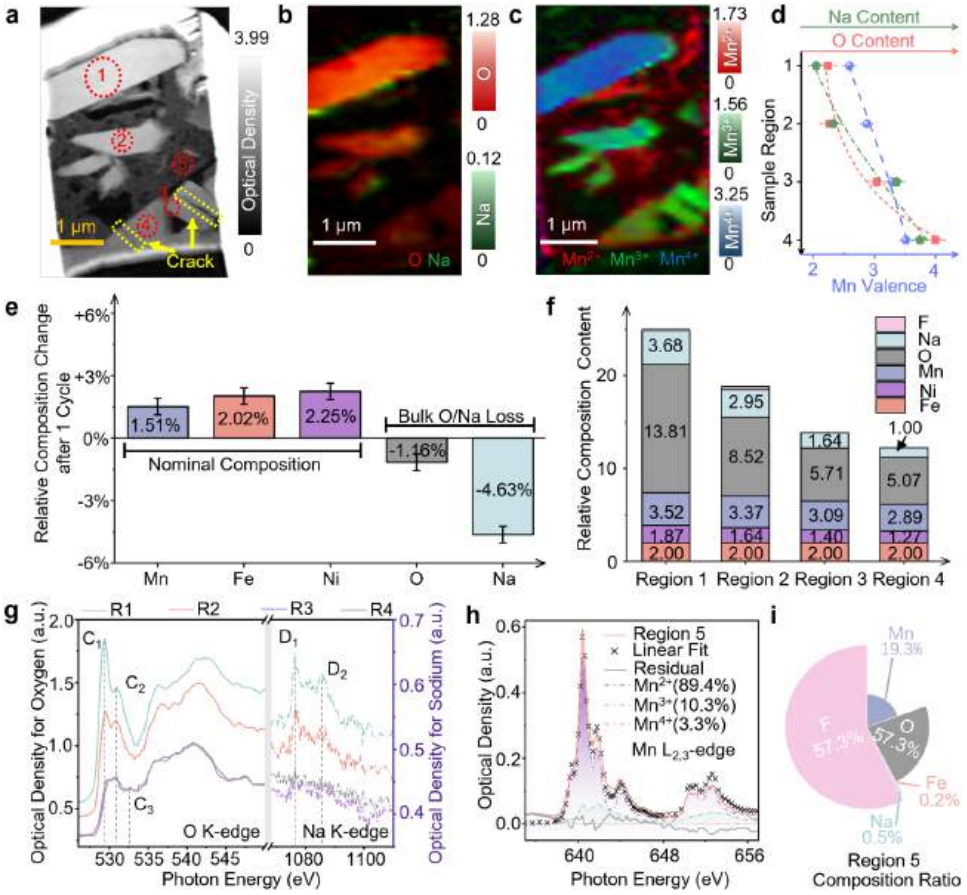

Figure 2. Conventional STXM and ptychography results of the slice 1-0 SoC at the O K-edge, Mn $L_{2,3}$-edge, F K-edge, Fe $L_{2,3}$-edge, Ni $L_{2,3}$-edge, and Na K-edge. (a) Averaged ptychography amplitude image from all elemental edges (converted to OD). (b) Color composite map of conventional STXM images from the O and Na K-edges. (c) Color composite map of conventional STXM images from Mn^{2+}, Mn^{3+}, and Mn^{4+} edges. (d) Trends of Mn valence states and the content of the O and Na across different sample regions. (e) Relative composition change of Mn, Fe, Ni, O, and Na after one cycle compared to pristine. (f) Quantitative XAS analysis at all edges in different regions of interest. (g) XAS spectra involving the O K-edge and Na K-edge in different regions of interest extracted from (a). (h) Mn $L_{2,3}$-edge XAS of region 5 with fitting to Mn^{2+}, Mn^{3+}, and Mn^{4+} reference spectra. (i) Elemental proportions of Mn, Fe, Ni, O, and Na in region 5.

To investigate the chemomechanical interplay in the NLNFM cathode, we milled the cathodes to a 200 nm thickness using a focused ion beam (FIB) for soft X-ray characterization. We compared several samples with different electrochemical histories, including discharged electrodes at 0% state of charge (SoC) after 1 cycle (1-0 SoC), at 0% SoC after 200 cycles (200-0 SoC), and at 50% SoC after 200 cycles (200-50 SoC). To shed light on the cathode's activation process, our first analysis focuses on the 1-0 SoC slice. Figure 2a displays the morphology of the 1-0 SoC sample imaged by using high-resolution STXM-based ptychography. This averaged amplitude image was acquired from the O K-edge, Mn $L_{2,3}$-edge, F K-edge, Fe $L_{2,3}$-edge, Ni $L_{2,3}$-edge, and Na K-edge. Quantitative analysis of the element concentration was performed over the entire sample. Interestingly, severe Na and O loss already occurs after the first cycle, featuring a decrease of 1.16% in the Na content and 4.63% in the O content compared with the nominal composition (Figures 2e and S4). The Na and O loss, in turn, leads to an increase of the relative concentrations of the transition metal cations. To further investigate the Na/O loss, five regions of interest, as annotated in Figure 2a, are selected. Regions 1−4 are particles of different sizes, while region 5 is primarily composed of PVDF. First, from the morphology perspective, particle 1 (large) appears to be structurally intact, while particles 3 and 4 (small) clearly exhibit straight and sharp-edged splits. Similarly, from Figure 2b,c, O, Na, and Mn^{4+} are unevenly concentrated in these regions. The small particles (2, 3, and 4) are characterized by more severe O and Na loss, accompanied by the formation of Mn^{3+} replacing Mn^{4+}. This is corroborated by the Pearson product-moment correlation coefficient (PPMCC) between Na and O over the entire slice, featuring a high value of 0.8975 (Figure S5). Moreover, the compositional statistics (Figure 2f) show that the content ratios of Na, Ni, Fe, Mn, and O in regions 1 to 4 are 6.18:1.89:2.00:3.52:13.80, 2.95:1.64:2.00:3.37:8.51, 1.51:1.27:2.00:2.84:5.24, and 1.09:1.40:2.00:3.09:5.71, respectively. Compared with the nominal ratio of 9:2:2:4:18, region 1 is the least affected, while regions 3 and 4 are the most affected, well aligned with the observed morphological damages, suggesting that Mn dissociation or Na/O loss may serve as the primary contributor to the observed performance degradation. It is worth noting that the distributions of Fe and Ni in particles 3 and 4 are quite uniform, contrasting the behavior of Mn and suggesting the different roles of these transition metal elements (Figures 2c and S6). In region 5, 2.2 $\times 10^{-6}$ mol/cm^2 of Mn was detected, accounting for 19.3% of the element content in the PVDF area (see Figure 2i). By

https://doi.org/10.1021/jacs.4c14571
J. Am. Chem. Soc. 2025, 147, 21375−21384

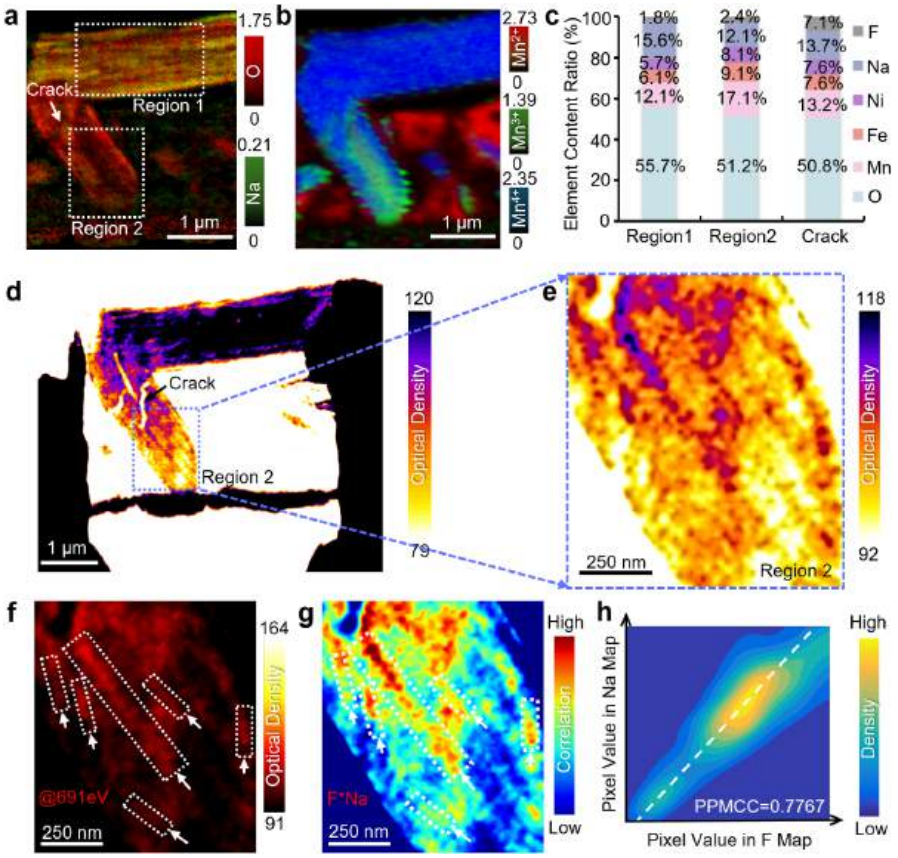

Figure 3. Morphological and chemical analysis of the 200-0 SoC Slice. (a) Color composite map showing the distribution of O and Na, with regions 1, 2, and the crack indicated by the white dashed boxes and the white arrow. (b) Color composite map of Mn^{2+}, Mn^{3+}, and Mn^{4+} distributions. (c) Elemental composition ratios for region 1, region 2, and the crack as indicated in (a). (d) Averaged ptychography amplitude image of slice 200-0 SoC from all elemental edges. (e) Magnified view of region 2 from (d). (f) Ptychography image of region 2 at 691 eV. (g) Result of multiplying the distributions of F and Na derived from ptychography data, with higher pixel values (closer to warm colors) indicating areas where Na and F coenrich. (h) Statistical correlation analysis of Na and F in region 2.

fitting the Mn L-edge spectrum over this region, it appears that Mn^{2+} accounts for 89.3% of the total Mn content in this area. This observation could be attributed to Mn dissolution and reprecipitation, likely driven by an acid-mediated attack under high-voltage conditions. This process is facilitated by HF generated through the hydrolysis of $NaPF_6$ or electrolyte decomposition at high voltage, which preferentially stabilizes Mn^{2+} in the reprecipitated phase.

We further extracted the O K-edge and Na K-edge spectra (Figure 2g) from the five regions of interest. While the overall O K-edge spectrum shape is similar to that in the pristine sample (Figure 1i), some interesting characteristics emerge. Specifically, the resonance peak ranges from 531.6 to 533.0 eV, and the C_3 peak is much less prominent in regions 3 and 4, where the loss of O/Na and the dissolution of Mn are the most significant. C_3 is in the same energy range as the signature of Na_2CO_3 observed in the pristine particle, yet it is much wider and weaker. This may be attributed to the change in TM-O bond strength caused by lattice distortion or mismatched oxygen, which could induce localized strain. Through a more in-depth analysis of a fully discharged slice and a 50% discharged slice, we identified that this peak is attributed to residual redox of O in the sample, resulting from the kinetic slowdown of Na intercalation (see the Charge Compensation Mechanism Section in Supporting Information). In contrast, the Na K-edge absorption spectra in the 1-0 SoC slice are consistent with those observed in the pristine particles. However, the Na signal is weaker in regions 3 and 4, likely due to the lower Na concentration resulting from hindered intercalation dynamics, which may contribute to stress accumulation. These results clearly suggest a close association of the loss of O and Na with the reduction and dissolution of Mn^{4+}, which could reprecipitate over the PVDF region in the form of Mn^{2+} species. In addition, there appears to be a particle size dependence, with the small particles undergoing more significant side reactions. The small particles are characterized by larger specific surface areas, leading to faster cathode-electrolyte interface (CEI) growth and making them more susceptible to the detrimental side reactions during the formation cycles, as elaborated above.

To study the chemical origins of the gradual long-term capacity fade following the first few formation cycles (see Figure 1j,k), we performed STXM over the O K-edge, Mn $L_{2,3}$-edge, F K-edge, Fe $L_{2,3}$-edge, Ni $L_{2,3}$-edge, and Na K-edge on a 200-50 SoC slice and a 200-0 SoC slice. Figures S7 and S8 show the morphology and elemental maps. The averaged XAS spectra over slices 1-0 SoC, 200-50 SoC, and 200−0 SoC were extracted for comparison (see Figures S9 and S10). Notably, in the 200-0 SoC slice, some large particles also show significant structural disintegration and display pronounced heterogeneity in electronic structure and mechanical stress. For example, region 2 of the 200-0 SoC slice (Figure 3a,b) shows substantial

https://doi.org/10.1021/jacs.4c14571
J. Am. Chem. Soc. 2025, 147, 21375−21384

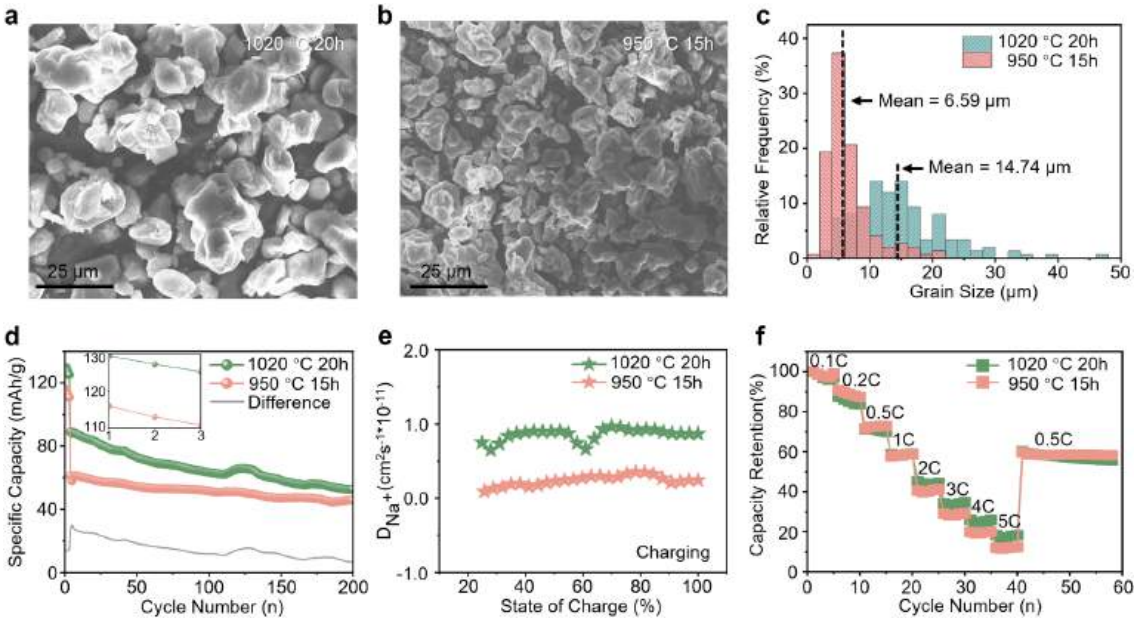

Figure 4. Morphology and electrochemical performance comparison of NLNFM cathode particles sintered at 1020 °C for 20 h and 950 °C for 15 h. (a) SEM image of NLNFM cathode particles sintered at 1020 °C for 20 h. (b) SEM image of NLNFM cathode particles sintered at 950 °C for 15 h. (c) Particle size distribution histogram for both sintering conditions. (d) Electrochemical performance plot for both materials (first 3 cycles at 0.1 C for activation, followed by long cycling at 1 C). (e) GITT results for M950 and M1020 in initial cycles. (f) Rate performance plot for both materials.

losses of O and Na, with Mn^{4+} being replaced by Mn^{3+}. In contrast, region 1 remained relatively intact. Interestingly, in the cracked regions, the cathode material also demonstrates notable compositional dissociation, with losses of O, Na, and Mn^{4+}, accompanied by a high concentration of Mn^{3+} (Figure 3c). Additionally, Figure S8b shows that the Fe and Ni content within the cracks is only slightly reduced (0.78×10^{-6} mol/cm^2 and 0.16×10^{-6} mol/cm^2, respectively) compared to region 2 on the same particle. This observation suggests that unlike in the 1-0 SoC slice, the cracks in the 200-0 SoC sample do not propagate completely through the thickness of the particle, featuring an irregular crack propagation pattern, likely due to progressive strain and stress accumulation.

To gain deeper insight, we employed high-resolution spectro-ptychography to investigate both the 200-0 SoC and 200-50 SoC slices at the O K-edge, Mn $L_{2,3}$-edge, F K-edge, Fe $L_{2,3}$-edge, Ni $L_{2,3}$-edge, and Na K-edge. Interestingly, in the amplitude map of the degraded larger particle (region 2 of the 200-0 SoC slice), we observed a grape-like structure consisting of spherical nanoparticles ranging from 20 to 70 nm in diameter (see Figure 3d,e). As shown in Figure 3f, this structure was more clearly revealed in the F K-edge averaged amplitude image (also visible in the F spectro-ptychography difference maps at 684.0 and 691.0 eV, Figure S11). Furthermore, elemental spatial correlation analysis (Figure 3g) indicated a strong correlation between Na and F at the locations of these spherical nanoparticles, with no evident correlation with the other elements in these regions (Figure S12a−c). Additionally, the overall statistical correlation in Figure 4h further supports the positive correlation between Na and F. Similar spherical nanoparticles were also observed in 200-50 SoC slices (Figure S13). These observations strongly suggest that these nanoparticles are NaF formed as a result of cathode degradation.

This is further corroborated by the XAS data (Figure S8c). In the O K-edge range, the severely degraded region 2 exhibits a more pronounced peak C_3 around 532.2 eV, indicating a higher presence of mismatched O. In the Na K-edge range, the peak B_2 labeled in Figure 1g is higher at 1082.3 eV. This peak is more prominent in the cracks and in region 2, where the degradation of the larger particles is more severe. It has been suggested that fluorine participates in the formation of CEI as NaF and PFO_x ions. The growth of NaF grains can lead to the loss of CEI protection, allowing solvents and impurities from the electrolyte to penetrate the cathode, causing accelerated degradation of the electrode material.[35] Moreover, the formation of cracks in the secondary particles during subsequent charge−discharge cycles exposes new cathode surfaces to the electrolyte, further compromising the performance and lifespan of the cathode.

Additionally, from the mapping results in Figure S11, it is evident that both regions 1 and 2 contain F, and the content analysis in Figure S8b reveals that the more severely degraded region 2 has a higher relative concentration of F, consistent with the spatial correlation analysis between F and Ni (Figure S14). Considering the bulk sensitivity of STXM, the high concentration of F species within the NLNFM particles in the 200-0SoC sample cannot be solely attributed to the CEI layer on the particle surface. This observation prompted us to consider the possible incorporation of F ions into the NLNFM lattice after extended cycling under a wide voltage range of 2.0 to 4.3 V. Therefore, we suggest that F incorporates into the lattice during extended cycling via defects and cracks, facilitated by oxygen loss and structural destabilization, driving structural evolution at both the lattice and particle levels. The heterogeneous growth orientation, rate, and distribution of these NaF particles can lead to stress accumulation and progressive crack development.

https://doi.org/10.1021/jacs.4c14571
J. Am. Chem. Soc. 2025, 147, 21375−21384

To validate the impact of particle-size-dependent degradation mechanisms on battery performance, we prepared two samples with identical composition but subjected to different sintering processes: one sintered at 950 °C for 15 h and the other at 1020 °C for 20 h, denoted as M950 and M1020, respectively. Figure S15 shows the XRD patterns of both materials, confirming that they exhibit the same lattice structure. Figure 4a,b presents SEM images of the two samples, while Figure 4c depicts the particle size distributions based on the statistical analysis of over 150 particles for each material. The average particle size of M1020 is 14.74 μm, compared to 6.59 μm for M950. Figure 4d displays the electrochemical performance over 200 cycles for both materials. In the first cycle, M1020 shows a higher discharge specific capacity compared to M950. During the first five cycles, the specific capacity difference between M1020 and M950 increases, but after the fifth cycle, this difference begins to decrease and continues to do so through the 200th cycle (Figure 4e). These results indicate that M1020 exhibits a degradation rate lower than that of M950 during the early formation cycles; however, M1020 undergoes more severe degradation over the long term. Despite this, M1020 maintains a higher specific capacity after 200 cycles compared to M950. Consistently, ex situ XRD measurements at different cycles (Figures S16−S19) reveal particle-size-dependent strain evolution, with small particles exhibiting significant strain changes during initial cycles and large particles showing more pronounced strain accumulation during extended cycling. This strain behavior aligns well with the proposed mechanism of chemical degradation driving mechanical stress development, highlighting the chemomechanical coupling pathway in NLNFM cathode materials.

Moreover, to explore the difference in sodium diffusion kinetics between the two materials, we employed the galvanostatic intermittent titration technique (GITT). GITT is typically used to probe sodium ion diffusion kinetics in battery materials.[36,37] However, the sodium diffusion coefficient, D_{Na^+}, derived from the GITT curve, reflects not only the intrinsic diffusion capacity but also the degree of side reactions, particularly during one of the early formation cycles.[38] In our GITT measurement (Figures 4e and S20,S21), the overall trend of D_{Na^+} upon charging/discharging in the initial cycles shows that M1020 has a higher diffusion capacity than M950, confirming that increasing the particle size enhances resistance to side reactions during the early cycle. Additionally, the rate capability tests (Figure 4f) reveal that larger particle sizes also provide a comparable rate performance to smaller particles. This suggests that larger particle sizes could provide benefits without compromising overall battery rate performance, which highlights the importance of optimizing the particle size distribution to achieve improved performance across different metrics.

A detailed analysis of the XRD patterns, together with selected electrochemical impedance spectroscopy (EIS) measurements at different states of charge (SoC) (Figures S22 and S23), indicates that the SoC range does not significantly affect the degradation rate of cathode materials with different particle sizes (see Analysis of the Impact of the SoC Range on Cathode Degradation in Supporting Information for a comprehensive discussion). This result implies that during the early cycles, M950, which contains a larger population of small particles, experienced more rapid degradation due to the lack of sufficient CEI protection. This led to a faster degradation rate for M950 in the initial cell formation phase. Similar trends have been reported in the literature, where smaller particles with higher surface area are associated with accelerated side reactions and uneven CEI coverage, ultimately exacerbating early-stage degradation.[39,40]

In contrast, smaller particles may promote earlier completion of CEI formation, effectively protecting the particles and leading to slower degradation. These observations suggest that controlling the particle size is a promising strategy for optimizing battery design and manufacturing. Appropriately increasing the particle size is particularly beneficial for the formation process and could enhance capacity retention without significantly jeopardizing rate performance.

CONCLUSION

We systematically investigated the degradation mechanisms of NLNFM cathode materials under high-voltage cycling using conventional spectro-STXM and high-spatial-resolution ptychography techniques. Our findings reveal that the degradation process of NLNFM involves the coupling of a range of chemical and mechanical processes, including Na/O loss, transition metal dissolution and precipitation, formation of cracks and NaF nanoparticles, and incorporation of F into the cathode lattice. By using the particle size as a decoupling parameter, we discovered that large and small particles undergo different chronic and acute degradation processes, respectively. Specifically, small particles experience severe capacity loss during the initial formation cycles due to insufficient CEI protection caused by their higher specific surface area. Conversely, large particles exhibit progressive degradation over long-term cycling, driven by intraparticle stress and heterogeneity.

Crucially, the primary trigger for NLNFM degradation at high voltage is the loss of oxygen, which is accompanied by the reduction and migration of Mn^{4+}, leading to sluggish Na intercalation and capacity loss. This oxygen loss inhibits the completion of the oxygen redox process during the latter stages of discharge, further exacerbating capacity fade. Additionally, F was observed to be incorporated into the NLNFM lattice during long-term degradation, progressively forming NaF nanoparticles. This process not only consumes Na resources but also destabilizes the CEI, leading to uneven interphase coverage and localized exposure of the cathode surface. The resulting inhomogeneous local stress in the NLNFM particles induces particle cracking, generating new surfaces that interact with the electrolyte, further destabilizing the CEI and accelerating degradation.

We propose that a multifaceted strategy is essential to mitigate the root causes of high-voltage degradation. Appropriately increasing the particle size can help mitigate the rapid capacity fade during the formation cycles, which could improve long-term cycling stability. Future efforts could focus on optimizing the particle size distribution to balance performance between the formation cycles and prolonged battery operation, thereby maximizing capacity retention.

Additionally, the distinct degradation processes in the early and later phases of cycling could also be directly optimized through targeted interventions. To combat the rapid capacity drop during the formation cycles, techniques such as surface modifications with protective coatings (e.g., carbon or oxide layers) or artificial SEI could be effective. Optimizing electrolyte composition to reduce surface side reactions also remains critical. For enhancing long-term cycling stability,

https://doi.org/10.1021/jacs.4c14571
J. Am. Chem. Soc. 2025, 147, 21375−21384

element doping (e.g., boron, magnesium, zinc, or tungsten) offers a promising avenue to improve structural stability and reduce oxygen loss.[21,41,42]

Moreover, designing nanostructured materials to accommodate stress and utilizing high-voltage stable electrolytes can further minimize oxygen loss and Mn^{4+} migration. Combining these approaches offers a comprehensive strategy to address the complex degradation mechanisms identified in this study.

■ ASSOCIATED CONTENT

Supporting Information

The Supporting Information is available free of charge at https://pubs.acs.org/doi/10.1021/jacs.4c14571.

Experimental section; electrochemical measurements; material characterization; data analysis; charge compensation mechanism; supporting figures and tables; references (PDF)

■ AUTHOR INFORMATION

Corresponding Authors

Bin Wu − *School of Materials Science and Engineering, Nanyang Technological University, Singapore 639798, Singapore*; Email: bin.wu@ntu.edu.sg

Jigang Zhou − *Canadian Light Source Inc, Saskatoon S7N 2 V3, Canada; GM Battery R&D, Warren, Michigan 48092, United States*; Email: jigang.zhou@gm.com

Yu-Guo Guo − *CAS Key Laboratory of Molecular Nanostructure and Nanotechnology, CAS Research/Education Center for Excellence in Molecular Sciences, Beijing National Laboratory for Molecular Sciences, Institute of Chemistry, Chinese Academy of Sciences (CAS), Beijing 100190, PR China*; orcid.org/0000-0003-0322-8476; Email: ygguo@iccas.ac.cn

Yijin Liu − *Walker Department of Mechanical Engineering, The University of Texas at Austin, Austin, Texas 78712, United States*; orcid.org/0000-0002-8417-2488; Email: liuyijin@utexas.edu

Authors

Tianxiao Sun − *Walker Department of Mechanical Engineering, The University of Texas at Austin, Austin, Texas 78712, United States*

Shimao Deng − *Walker Department of Mechanical Engineering, The University of Texas at Austin, Austin, Texas 78712, United States*

Yu-Jie Guo − *CAS Key Laboratory of Molecular Nanostructure and Nanotechnology, CAS Research/Education Center for Excellence in Molecular Sciences, Beijing National Laboratory for Molecular Sciences, Institute of Chemistry, Chinese Academy of Sciences (CAS), Beijing 100190, PR China*

Ji-Lei Shi − *CAS Key Laboratory of Molecular Nanostructure and Nanotechnology, CAS Research/Education Center for Excellence in Molecular Sciences, Beijing National Laboratory for Molecular Sciences, Institute of Chemistry, Chinese Academy of Sciences (CAS), Beijing 100190, PR China*; orcid.org/0000-0003-2887-2620

Xing Zhang − *CAS Key Laboratory of Molecular Nanostructure and Nanotechnology, CAS Research/Education Center for Excellence in Molecular Sciences, Beijing National Laboratory for Molecular Sciences, Institute of Chemistry, Chinese Academy of Sciences (CAS), Beijing 100190, PR China*; orcid.org/0000-0002-5840-4142

Xiaofeng Shi − *School of Environment and Safety Engineering, North University of China, Taiyuan 030051, PR China*

Guannan Qian − *Walker Department of Mechanical Engineering, The University of Texas at Austin, Austin, Texas 78712, United States*

Jian Wang − *Canadian Light Source Inc, Saskatoon S7N 2 V3, Canada*; orcid.org/0000-0001-5184-7023

Piero Pianetta − *Stanford Synchrotron Radiation Lightsource, SLAC National Accelerator Laboratory, Menlo Park, Californias 94025, United States*

Complete contact information is available at: https://pubs.acs.org/10.1021/jacs.4c14571

Author Contributions

○T.S., B.W., and S.D. contributed equally to this work.

Notes

The authors declare no competing financial interest.

■ ACKNOWLEDGMENTS

This research utilized the Canadian Light Source's SM beamline for both conventional STXM and ptychography measurements. Laboratory XRD and SEM analyses were conducted at the Texas Materials Institute at the University of Texas at Austin. The work at UT Austin was supported by the NSF under Grant No. CBET-2349665. The work at Nanyang Technological University was supported by the National Research Foundation, Singapore, and A*STAR (Agency for Science, Technology and Research) under its LCER Phase 2 Programme 1st Emerging Technology (Award No. U2411D4006), as well as the Key Laboratory of Functional Inorganic Material Chemistry (Heilongjiang University), Ministry of Education, P.R. China. The work at the Institute of Chemistry, Chinese Academy of Sciences (CAS), was supported by the Basic Science Center Project of National Natural Science Foundation of China (Grant No. 52388201) and the National Natural Science Foundation of China (Grant No. 22309189).

■ REFERENCES

(1) Wan, H.; Xu, J.; Wang, C. Designing Electrolytes and Interphases for High-Energy Lithium Batteries. *Nat. Rev. Chem.* **2024**, *8* (1), 30−44.

(2) Tembo, P. M.; Dyer, C.; Subramanian, V. Lithium-Ion Battery Recycling—a Review of the Material Supply and Policy Infrastructure. *NPG Asia Mater.* **2024**, *16* (1), 43.

(3) Lv, S.; Ma, X.; Ke, S.; Wang, Y.; Ma, T.; Yuan, S.; Jin, Z.; Zuo, J.-L. Metal-Coordinated Covalent Organic Frameworks as Advanced Bifunctional Hosts for Both Sulfur Cathodes and Lithium Anodes in Lithium−Sulfur Batteries. *J. Am. Chem. Soc.* **2024**, *146* (13), 9385−9394.

(4) Ryu, H.-H.; Lim, H.-W.; Lee, S. G.; Sun, Y.-K. Near-Surface Reconstruction in Ni-Rich Layered Cathodes for High-Performance Lithium-Ion Batteries. *Nat. Energy* **2024**, *9*, 47.

(5) Liang, H.-J.; Liu, H.-H.; Zhao, X.-X.; Gu, Z.-Y.; Yang, J.-L.; Zhang, X.-Y.; Liu, Z.-M.; Tang, Y.-Z.; Zhang, J.-P.; Wu, X.-L. Electrolyte Chemistry toward Ultrawide-Temperature (−25 to 75 °C) Sodium-Ion Batteries Achieved by Phosphorus/Silicon-Synergistic Interphase Manipulation. *J. Am. Chem. Soc.* **2024**, *146* (11), 7295−7304.

(6) Wu, H.; Hao, J.; Jiang, Y.; Jiao, Y.; Liu, J.; Xu, X.; Davey, K.; Wang, C.; Qiao, S.-Z. Alkaline-Based Aqueous Sodium-Ion Batteries for Large-Scale Energy Storage. *Nat. Commun.* **2024**, *15* (1), 575.

(7) Zhang, B.; Dugas, R.; Rousse, G.; Rozier, P.; Abakumov, A. M.; Tarascon, J.-M. Insertion Compounds and Composites Made by Ball Milling for Advanced Sodium-Ion Batteries. *Nat. Commun.* **2016**, *7* (1), 10308.
(8) Wang, Q.; Zhou, D.; Zhao, C.; Wang, J.; Guo, H.; Wang, L.; Yao, Z.; Wong, D.; Schuck, G.; Bai, X.; Lu, J.; Wagemaker, M. Fast-Charge High-Voltage Layered Cathodes for Sodium-Ion Batteries. *Nat. Sustain.* **2024**, *7* (3), 338−347.
(9) Zhao, C.; Ding, F.; Lu, Y.; Chen, L.; Hu, Y.-S. High-Entropy Layered Oxide Cathodes for Sodium-Ion Batteries. *Angew. Chem. Int. Ed.* **2020**, *59* (1), 264−269.
(10) Yu, X. Releasing Oxygen from the Bulk. *Nat. Energy* **2021**, *6* (6), 572−573.
(11) Ko, W.; Cho, M.-K.; Kang, J.; Park, H.; Ahn, J.; Lee, Y.; Lee, S.; Lee, S.; Heo, K.; Hong, J.; Yoo, J.-K.; Kim, J. Exceptionally Increased Reversible Capacity of O3-Type NaCrO2 Cathode by Preventing Irreversible Phase Transition. *Energy Storage Mater.* **2022**, *46*, 289−299.
(12) Kim, J. C.; Kwon, D.-H.; Yang, J. H.; Kim, H.; Bo, S.-H.; Wu, L.; Kim, H.; Seo, D.-H.; Shi, T.; Wang, J.; Zhu, Y.; Ceder, G. Direct Observation of Alternating Octahedral and Prismatic Sodium Layers in O3-Type Transition Metal Oxides. *Adv. Energy Mater.* **2020**, *10* (31), 2001151.
(13) Cui, T.; Liu, L.; Xiang, Y.; Sheng, C.; Li, X.; Fu, Y. Facilitating an Ultrastable O3-Type Cathode for 4.5 V Sodium-Ion Batteries via a Dual-Reductive Coupling Mechanism. *J. Am. Chem. Soc.* **2024**, *146* (20), 13924−13933.
(14) Yu, T.-Y.; Ryu, H.-H.; Han, G.; Sun, Y.-K. Understanding the Capacity Fading Mechanisms of O3-Type Na[Ni0.5Mn0.5]O2 Cathode for Sodium-Ion Batteries. *Adv. Energy Mater.* **2020**, *10* (37), 2001609.
(15) Sun, L.; Wu, Z.; Hou, M.; Ni, Y.; Sun, H.; Jiao, P.; Li, H.; Zhang, W.; Zhang, L.; Zhang, K.; Cheng, F.; Chen, J. Unraveling and Suppressing the Voltage Decay of High-Capacity Cathode Materials for Sodium-Ion Batteries. *Energy Environ. Sci.* **2024**, *17* (1), 210−218.
(16) Wang, X.; Zhang, Q.; Zhao, C.; Li, H.; Zhang, B.; Zeng, G.; Tang, Y.; Huang, Z.; Hwang, I.; Zhang, H.; Zhou, S.; Qiu, Y.; Xiao, Y.; Cabana, J.; Sun, C.-J.; Amine, K.; Sun, Y.; Wang, Q.; Xu, G.-L.; Gu, L.; Qiao, Y.; Sun, S.-G. Achieving a High-Performance Sodium-Ion Pouch Cell by Regulating Intergrowth Structures in a Layered Oxide Cathode with Anionic Redox. *Nat. Energy* **2024**, *9* (2), 184−196.
(17) Kubota, K.; Fujitani, N.; Yoda, Y.; Kuroki, K.; Tokita, Y.; Komaba, S. Impact of Mg and Ti Doping in O3 Type NaNi1/2Mn1/2O2 on Reversibility and Phase Transition during Electrochemical Na Intercalation. *J. Mater. Chem. A* **2021**, *9* (21), 12830−12844.
(18) You, Y.; Xin, S.; Asl, H. Y.; Li, W.; Wang, P.-F.; Guo, Y.-G.; Manthiram, A. Insights into the Improved High-Voltage Performance of Li-Incorporated Layered Oxide Cathodes for Sodium-Ion Batteries. *Chem* **2018**, *4* (9), 2124−2139.
(19) Mu, L.; Feng, X.; Kou, R.; Zhang, Y.; Guo, H.; Tian, C.; Sun, C.-J.; Du, X.-W.; Nordlund, D.; Xin, H. L.; Lin, F. Deciphering the Cathode−Electrolyte Interfacial Chemistry in Sodium Layered Cathode Materials. *Adv. Energy Mater.* **2018**, *8* (34), 1801975.
(20) Tang, Y.; Zhang, Q.; Zuo, W.; Zhou, S.; Zeng, G.; Zhang, B.; Zhang, H.; Huang, Z.; Zheng, L.; Xu, J.; Yin, W.; Qiu, Y.; Xiao, Y.; Zhang, Q.; Zhao, T.; Liao, H.-G.; Hwang, I.; Sun, C.-J.; Amine, K.; Wang, Q.; Sun, Y.; Xu, G.-L.; Gu, L.; Qiao, Y.; Sun, S.-G. Sustainable Layered Cathode with Suppressed Phase Transition for Long-Life Sodium-Ion Batteries. *Nat. Sustain.* **2024**, *7* (3), 348−359.
(21) Guo, Y.-J.; Wang, P.-F.; Niu, Y.-B.; Zhang, X.-D.; Li, Q.; Yu, X.; Fan, M.; Chen, W.-P.; Yu, Y.; Liu, X.; Meng, Q.; Xin, S.; Yin, Y.-X.; Guo, Y.-G. Boron-Doped Sodium Layered Oxide for Reversible Oxygen Redox Reaction in Na-Ion Battery Cathodes. *Nat. Commun.* **2021**, *12* (1), 5267.
(22) Ould, D. M. C.; Menkin, S.; Smith, H. E.; Riesgo-Gonzalez, V.; Jónsson, E.; O'Keefe, C. A.; Coowar, F.; Barker, J.; Bond, A. D.; Grey, C. P.; Wright, D. S. Sodium Borates: Expanding the Electrolyte Selection for Sodium-Ion Batteries. *Angew. Chem. Int. Ed.* **2022**, *61* (32), No. e202202133.
(23) Barnes, P.; Smith, K.; Parrish, R.; Jones, C.; Skinner, P.; Storch, E.; White, Q.; Deng, C.; Karsann, D.; Lau, M. L.; Dumais, J. J.; Dufek, E. J.; Xiong, H. A Non-Aqueous Sodium Hexafluorophosphate-Based Electrolyte Degradation Study: Formation and Mitigation of Hydrofluoric Acid. *J. Power Sources* **2020**, *447*, 227363.
(24) Liu, Y.; Wang, J.; Shi, Q.; Yan, M.; Zhao, S.; Feng, W.; Qi, R.; Xu, J.; Luo, J.; Zhang, J.; Zhao, Y. A Stress Self-Adaptive Structure to Suppress the Chemo-Mechanical Degradation for High Rate and Ultralong Cycle Life Sodium Ion Batteries. *Angew. Chem. Int. Ed.* **2023**, *62* (29), No. e202303875.
(25) Sun, T.; Sun, G.; Yu, F.; Mao, Y.; Tai, R.; Zhang, X.; Shao, G.; Wang, Z.; Wang, J.; Zhou, J. Soft X-Ray Ptychography Chemical Imaging of Degradation in a Composite Surface-Reconstructed Li-Rich Cathode. *ACS Nano* **2021**, *15* (1), 1475−1485.
(26) Wu, M.; Zhang, G.; Tong, H.; Liu, X.; Du, L.; Chen, N.; Wang, J.; Sun, T.; Regier, T.; Sun, S. C. (II) Oxide Nanosheets with Rich Oxygen Vacancies as Highly Efficient Bifunctional Catalysts for Ultra-Stable Rechargeable Zn-Air Flow Battery. *Nano Energy* **2021**, *79*, 105409.
(27) Liu, Z.; Zeng, Y.; Tan, J.; Wang, H.; Zhu, Y.; Geng, X.; Guttmann, P.; Hou, X.; Yang, Y.; Xu, Y.; Cloetens, P.; Zhou, D.; Wei, Y.; Lu, J.; Li, J.; Liu, B.; Winter, M.; Kostecki, R.; Lin, Y.; He, X. Revealing the Degradation Pathways of Layered Li-Rich Oxide Cathodes. *Nat. Nanotechnol.* **2024**, *19*, 1821.
(28) Man, M. K. L.; Margiolakis, A.; Deckoff-Jones, S.; Harada, T.; Wong, E. L.; Krishna, M. B. M.; Madéo, J.; Winchester, A.; Lei, S.; Vajtai, R.; Ajayan, P. M.; Dani, K. M. Imaging the Motion of Electrons across Semiconductor Heterojunctions. *Nat. Nanotechnol.* **2017**, *12* (1), 36−40.
(29) Ma, C.; Alvarado, J.; Xu, J.; Clément, R. J.; Kodur, M.; Tong, W.; Grey, C. P.; Meng, Y. S. Exploring Oxygen Activity in the High Energy P2-Type Na0.78Ni0.23Mn0.69O2 Cathode Material for Na-Ion Batteries. *J. Am. Chem. Soc.* **2017**, *139* (13), 4835−4845.
(30) Wu, J.; Shen, Z.; Yang, W. Redox Mechanism in Na-Ion Battery Cathodes Probed by Advanced Soft X-Ray Spectroscopy. *Front. Chem.* **2020**, *8*, 8.
(31) Li, J.; Liu, J.; Sun, Q.; Banis, M. N.; Sun, X.; Sham, T.-K. Tracking the Effect of Sodium Insertion/Extraction in Amorphous and Anatase TiO2 Nanotubes. *J. Phys. Chem. C* **2017**, *121* (21), 11773−11782.
(32) McIntosh, G. J.; Chan, A. Probing Hydrogen Bonding Interactions and Impurity Intercalation in Gibbsite Using Experimental and Theoretical XANES Spectroscopy. *Phys. Chem. Chem. Phys.* **2018**, *20* (37), 24033−24044.
(33) Neuville, D. R.; Cormier, L.; Flank, A. M.; Prado, R. J.; Lagarde, P. Na K-edge XANES spectra of minerals and glasses. *Eur. J. Mineral.* **2004**, *16* (5), 809−816.
(34) Jiang, N.; Su, D.; Spence, J. C. H.; Zhou, S.; Qiu, J. Electron Energy Loss Spectroscopy of Na in Na, Na2O, and Silicate Glasses. *J. Mater. Res.* **2008**, *23* (9), 2467−2471.
(35) DiLecce, D.; Marangon, V.; Isaacs, M.; Palgrave, R.; Shearing, P. R.; Hassoun, J. Degradation of Layered Oxide Cathode in a Sodium Battery: A Detailed Investigation by X-Ray Tomography at the Nanoscale. *Small Methods* **2021**, *5* (10), 2100596.
(36) Wang, W.; Gang, Y.; Hu, Z.; Yan, Z.; Li, W.; Li, Y.; Gu, Q.-F.; Wang, Z.; Chou, S.-L.; Liu, H.-K.; Dou, S.-X. Reversible Structural Evolution of Sodium-Rich Rhombohedral Prussian Blue for Sodium-Ion Batteries. *Nat. Commun.* **2020**, *11* (1), 980.
(37) Zuo, W.; Liu, X.; Qiu, J.; Zhang, D.; Xiao, Z.; Xie, J.; Ren, F.; Wang, J.; Li, Y.; Ortiz, G. F.; Wen, W.; Wu, S.; Wang, M.-S.; Fu, R.; Yang, Y. Engineering Na ± Layer Spacings to Stabilize Mn-Based Layered Cathodes for Sodium-Ion Batteries. *Nat. Commun.* **2021**, *12* (1), 4903.
(38) Cui, Z. H.; Guo, X. X.; Li, H. Equilibrium Voltage and Overpotential Variation of Nonaqueous Li−O2 Batteries Using the Galvanostatic Intermittent Titration Technique. *Energy Environ. Sci.* **2015**, *8* (1), 182−187.
(39) Li, W.; Dolocan, A.; Oh, P.; Celio, H.; Park, S.; Cho, J.; Manthiram, A. Dynamic Behaviour of Interphases and Its Implication

on High-Energy-Density Cathode Materials in Lithium-Ion Batteries. *Nat. Commun.* **2017**, *8* (1), 14589.
(40) Wagner, A. C.; Bohn, N.; Geßwein, H.; Neumann, M.; Osenberg, M.; Hilger, A.; Manke, I.; Schmidt, V.; Binder, J. R. Hierarchical Structuring of NMC111-Cathode Materials in Lithium-Ion Batteries: An In-Depth Study on the Influence of Primary and Secondary Particle Sizes on Electrochemical Performance. *ACS Appl. Energy Mater.* **2020**, *3* (12), 12565−12574.
(41) Ding, Q.; Zheng, W.; Zhao, A.; Zhao, Y.; Chen, K.; Zhou, X.; Zhang, H.; Li, Q.; Ai, X.; Yang, H.; Fang, Y.; Cao, Y. W-Doping Induced Efficient Tunnel-to-Layered Structure Transformation of Na0.44Mn1-WO2: Phase Evolution, Sodium-Storage Properties, and Moisture Stability. *Adv. Energy Mater.* **2023**, *13* (21), 2203802.
(42) Lai, Y.; Xie, H.; Li, P.; Li, B.; Zhao, A.; Luo, L.; Jiang, Z.; Fang, Y.; Chen, S.; Ai, X.; Xia, D.; Cao, Y. Ion-Migration Mechanism: An Overall Understanding of Anionic Redox Activity in Metal Oxide Cathodes of Li/Na-Ion Batteries. *Adv. Mater.* **2022**, *34* (47), 2206039.

https://doi.org/10.1021/jacs.4c14571
J. Am. Chem. Soc. 2025, 147, 21375−21384